ACSNANO

www.acsnano.org

ARTICLE

Manipulation of Self-Assembled Nanostructure Dimensions in Molecular Janus Particles

Hao Liu,[†] Jiancheng Luo,[†] Wenpeng Shan,[†] Dong Guo,[†] Jing Wang,[†] Chih-Hao Hsu,[†] Mingjun Huang,[†] Wei Zhang,[†] Bernard Lotz,[‡] Wen-Bin Zhang,[§] Tianbo Liu,*[,†] Kan Yue,*[,†] and Stephen Z. D. Cheng*[,†]

[†]Department of Polymer Science, College of Polymer Science and Polymer Engineering, The University of Akron, Akron, Ohio 44325, United States

[‡]Institut Charles Sadron, CNRS, Université de Strasbourg, 23, Rue du Lœss, 67034 Strasbourg, France

[§]Key Laboratory of Polymer Chemistry & Physics of Ministry of Education, Center for Soft Matter Science and Engineering, College of Chemistry and Molecular Engineering, Peking University, Beijing 100871, China

Supporting Information

ABSTRACT: The ability to manipulate self-assembly of molecular building blocks is the key to achieving precise "bottom-up" fabrications of desired nanostructures. Herein, we report a rational design, facile synthesis, and self-assembly of a series of molecular Janus particles (MJPs) constructed by chemically linking α-Keggin-type polyoxometalate (POM) nanoclusters with functionalized polyhedral oligomeric silsesquioxane (POSS) cages. Diverse nanostructures were obtained by tuning secondary interactions among the building blocks and solvents *via* three factors: solvent polarity, surface functionality of POSS derivatives, and molecular topology. Self-assembled morphologies of KPOM-BPOSS (B denotes isobutyl groups) were found dependent on solvent polarity. In acetonitrile/water mixtures with a high dielectric constant, colloidal nanoparticles with nanophase-separated internal lamellar structures quickly formed, which gradually turned into one-dimensional nanobelt crystals upon aging, while stacked crystalline lamellae were dominantly observed in less polar methanol/chloroform solutions. When the crystallizable BPOSS was replaced with noncrystallizable cyclohexyl-functionalized CPOSS, the resulting KPOM-CPOSS also formed colloidal spheres; however, it failed to further evolve into crystalline nanobelt structures. In less polar solvents, KPOM-CPOSS crystallized into isolated two-dimensional nanosheets, which were composed of two inner crystalline layers of Keggin POM covered by two monolayers of amorphous CPOSS. In contrast, self-assembly of KPOM-2BPOSS was dominated by crystallization of the BPOSS cages, which was hardly sensitive to solvent polarity. The BPOSS cages formed the crystalline inner bilayer, sandwiched by two outer layers of Keggin POM clusters. These results illustrate a rational strategy to purposely fabricate self-assembled nanostructures with diverse dimensionality from MJPs with controlled molecular composition and topology.

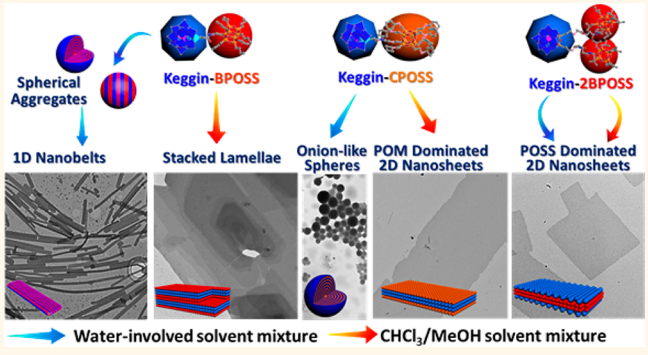

KEYWORDS: *Janus particles, self-assembly, nanobelts, nanosheets, polyoxometalates*

Macroscopic properties of materials are critically dependent on chemical compositions and packing schemes of atomic/molecular building blocks and also their hierarchical structures at different length scales.[1−3] In the past few decades, self-assembling materials with sophisticated multiple-level structures[4−6] have facilitated progress in energy,[7,8] electronics,[9,10] optics,[11,12] disease diagnosis, and clinical therapy.[13−15] However, manipulating the self-assembly of specifically designed building blocks to form predictable packing and ordered hierarchical structures remains a grand challenge.[16,17] Precise controls over the noncovalent or secondary interactions among the building blocks on different dimensions may be achieved by tuning primary chemical compositions.[18−20] As a model system to study the effects of versatile secondary interactions on controlled formation of nanostructures, "Janus grains"[21,22] have recently attracted extensive interest. A typical Janus grain consists of thermodynamically incompatible subunits associated with symmetry breaking in geometry and/or chemical affinity.[23−28] The relationships among the primary chemical structures, secondary interactions, and self-assembly behaviors have been vigorously studied by investigating both the intrinsic (*i.e.*, surface

Received: February 22, 2016
Accepted: June 23, 2016
Published: June 23, 2016

DOI: 10.1021/acsnano.6b01336
ACS Nano 2016, 10, 6585−6596

chemistry,[29,30] molecular shape,[31,32] size,[33,34] symmetry[23,35]) and external parameters (*i.e.*, solvent composition,[36] temperature,[37,38] concentration[39]).

Down to the molecular level, molecular Janus particles (MJPs),[23,40−42] also being viewed as "molecular Janus grains", are nanosized amphiphilic molecules with rigid 3D conformation. MJPs can be prepared as individual giant molecules using molecular nanoparticles (MNPs)[17,43] or so-called "nanoatoms",[44] as the building blocks, which are shape- and volume-persistent nanoscale objects with precisely defined molecular symmetry and surface functionalities. The explored library of MNPs includes derivatives of polyhedral oligomeric silsesquioxanes (POSS),[45−48] [60]fullerene (C_{60}),[49] polyoxometalates (POMs),[50−54] and folded protein domains.[55,56] Solution self-assembly behaviors of MJPs are determined by the relative solubility of their different components in a specific solvent. When selective solubility is introduced, self-assembled structures of the MJPs will be initiated. For instance, by subtly selecting appropriate solvents, dumbbell-shaped MJPs based on a pair of distinctly functionalized POSS cages could form either 3D bulk crystals with alternating lamellar structures[23] or 2D bilayered crystalline nanosheets with uniform thickness.[42] Very recently, a filled honeycomb structure formed by nanophase separation between Wells−Dawson-type POM and BPOSS subunits in MJP was reported.[57] It is thus intriguing to further advance knowledge about the self-assembly of such precisely defined MJPs and reveal unconventional self-assembled nanostructures as well as the formation mechanisms. Despite the previous reports, it remains largely unclear how to manipulate self-assembly of MJPs *via* rational molecular design and controlled experimental conditions to fabricate diverse nanostructures with tunable dimensionality and unexpected functions.

In this article, we report a systematic investigation toward the manipulation of nanostructure dimensions from a series of MJPs based on functionalized POSS derivatives and α-Keggin POM clusters formed in solution. Specifically, two hydrophobic POSS derivatives, crystalline isobutyl-substituted BPOSS and noncrystalline cyclohexyl-substituted CPOSS (Figure 1), were covalently tethered to a hydrophilic, crystalline Keggin POM cluster to build the MJPs. Since the size of an individual Keggin POM cluster is slightly larger than that of a POSS cage, the Keggin POMs are able to dominate the ordered structural formation of KPOM-BPOSS MJP. By selecting solvents with different dielectric constants (ε) or polarity, we can manipulate electrostatic interactions among the negatively charged POMs and their counterions[58−60] *via* different degrees of solvation, which dictate the formation of ordered nanostructures. Similar solvent polarity and size effects were also observed for KPOM-CPOSS. Interestingly, the amorphous nature of CPOSS cages also exhibits significant influence on the self-assembled structures. On the other hand, for KPOM-2BPOSS, the doubled number of BPOSS cages switches the roles of determining the ordered structures in these two MNPs. Self-assembly behaviors of KPOM-2BPOSS are found to be insensitive to solvent polarity. These results indicate that the distinct secondary interactions of the MNPs and the variations in molecular topology are able to provide controlled variables to manipulate morphologies and dimensions of the assembled nanostructures of the resulting MJPs. They offer additional guidance in designing nanomaterials with controllable structures, dimension, and functions *via* selective thermodynamic driving forces and kinetic pathways.

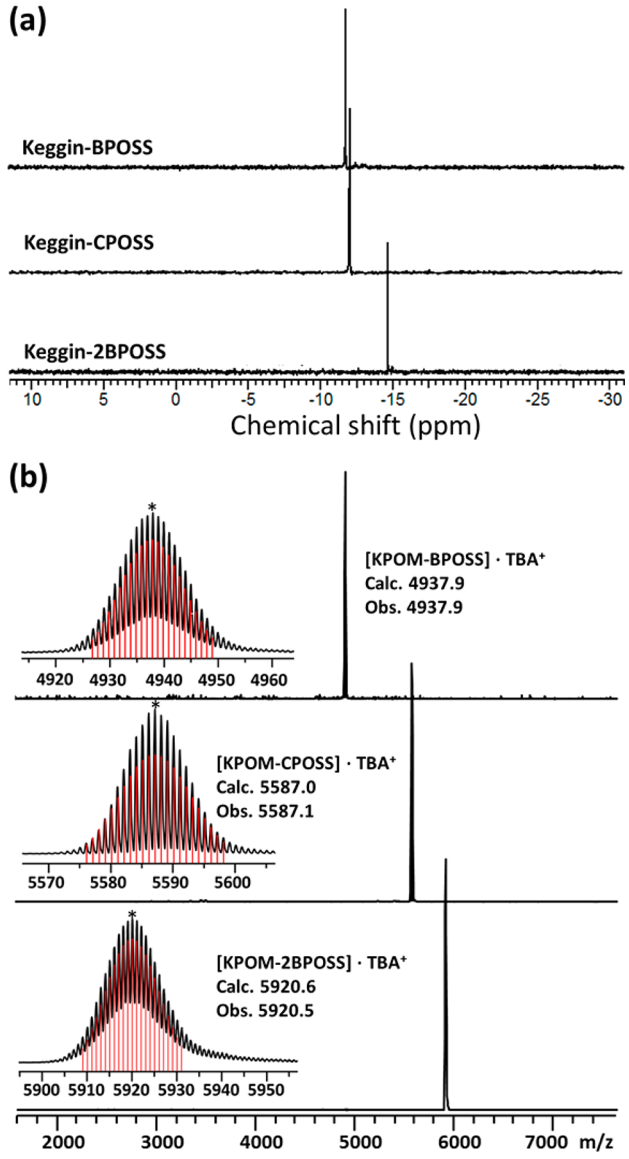

Figure 1. (a) ^{31}P NMR spectra and (b) MALDI-TOF mass spectra of KPOM-BPOSS, KPOM-CPOSS, and KPOM-2BPOSS. The red lines are simulated isotope patterns based on their molecular formulas. The starred peaks represent the 100% normalized intensity for the three samples.

RESULTS AND DISCUSSION

Molecular Design and Synthesis of KPOM-BPOSS, KPOM-CPOSS, and KPOM-2BPOSS. Scheme 1 illustrates the synthetic routes of three MJPs based on Keggin POM clusters and functionalized POSS cages. Chemical modifications of the Keggin POM clusters demand partial decomposition of the pristine cluster structure and result in lacunary Keggin POM derivatives with one or more missing tungsten atoms.[61] The remaining cavity possesses highly reactive oxygen atoms, and thus, it can be filled with diverse organic ligands (*e.g.*, compounds with organostannyl,[62] organogermyl,[63] and organosilyl groups[64]) to introduce reactive groups (*e.g.*, carboxylic acid groups or thiol groups) onto the Keggin POM clusters.

Conjugation of BPOSS/CPOSS cages with Keggin POM clusters can thus be readily achieved. We first reacted a monovacant Keggin POM precursor (with a molecular formula $[\alpha\text{-}PW_{11}O_{39}]^{7-}$) with 3-trichlorostannylpropanoic acid or 3-

DOI: 10.1021/acsnano.6b01336
ACS Nano 2016, 10, 6585−6596

Scheme 1. Synthetic Routes and Chemical Structures of KPOM-BPOSS, KPOM-CPOSS, and KPOM-2BPOSS[a]

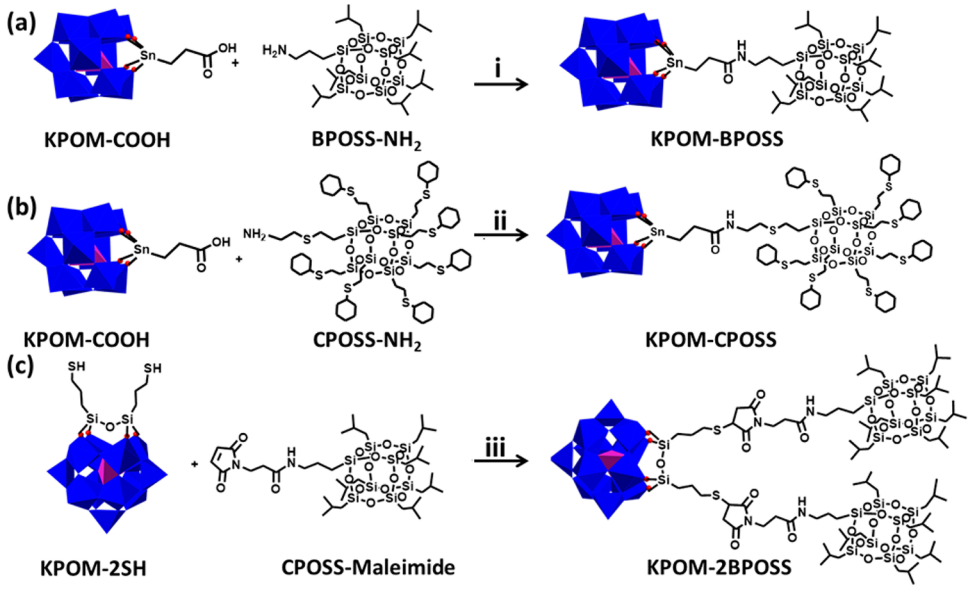

[a]Reagents and conditions: (i) EEDQ, acetonitrile/THF (v/v = 1/1), 80 °C, 91%; (ii) EEDQ, acetonitrile/THF (v/v = 1/1), 80 °C, 89%; (iii) catalytic amount of triethylamine, acetonitrile/THF (v/v = 1/1), 80 °C, 85%. Counterions are omitted for clarity.

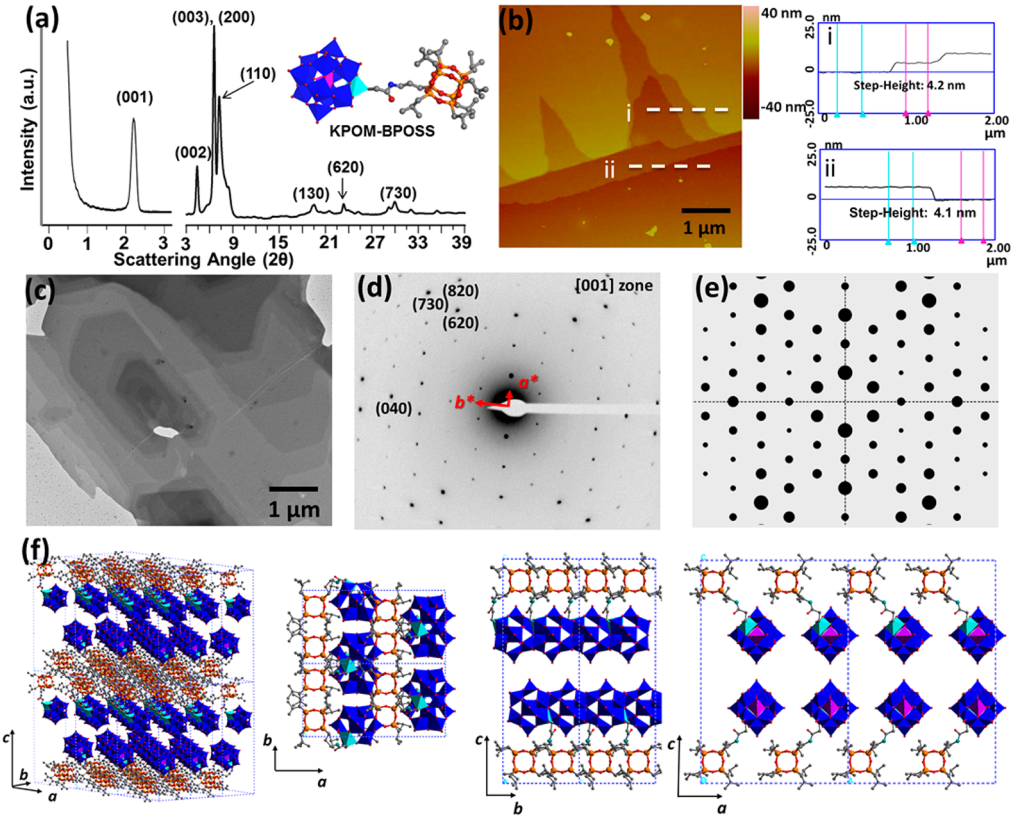

Figure 2. (a) SAXS and WAXD patterns of bulk crystals of KPOM-BPOSS. Inset shows the chemical structure model of KPOM-BPOSS. (b) AFM height measurements of the flat-on single crystals. The step-height analysis corresponds to traces along the white dashed lines. (c) Bright-field TEM image of the flat-on crystals. (d) Selected area electron diffraction patterns of the lamellar crystals in (c) along the [001] zone. (e) Computer-simulated electron diffraction patterns along the [001] zone. (f) The perspective views of the simulated orthorhombic crystal lattices (3 × 3 × 2) and the projections of *ab*-, *bc*-, and *ac*-planes for two lattices. TBA counterions are omitted for clarity.

mercaptopropyltrimethoxysilane to prepare KPOM-COOH[65] and KPOM-2SH,[64] respectively, as the intermediates for further conjugation. KPOM-BPOSS and KPOM-CPOSS were then prepared through the *N*-ethoxycarbonyl-2-ethoxy-1,2-dihydroquinoline (EEDQ)-mediated amidation[66] between KPOM-COOH and BPOSS-NH_2/CPOSS-NH_2 at increased temperatures in a mixed solvent of THF/acetonitrile (v/v = 1/1) (Scheme 1a,b). On the other hand, the highly efficient "thiol–

DOI: 10.1021/acsnano.6b01336
ACS Nano 2016, 10, 6585–6596

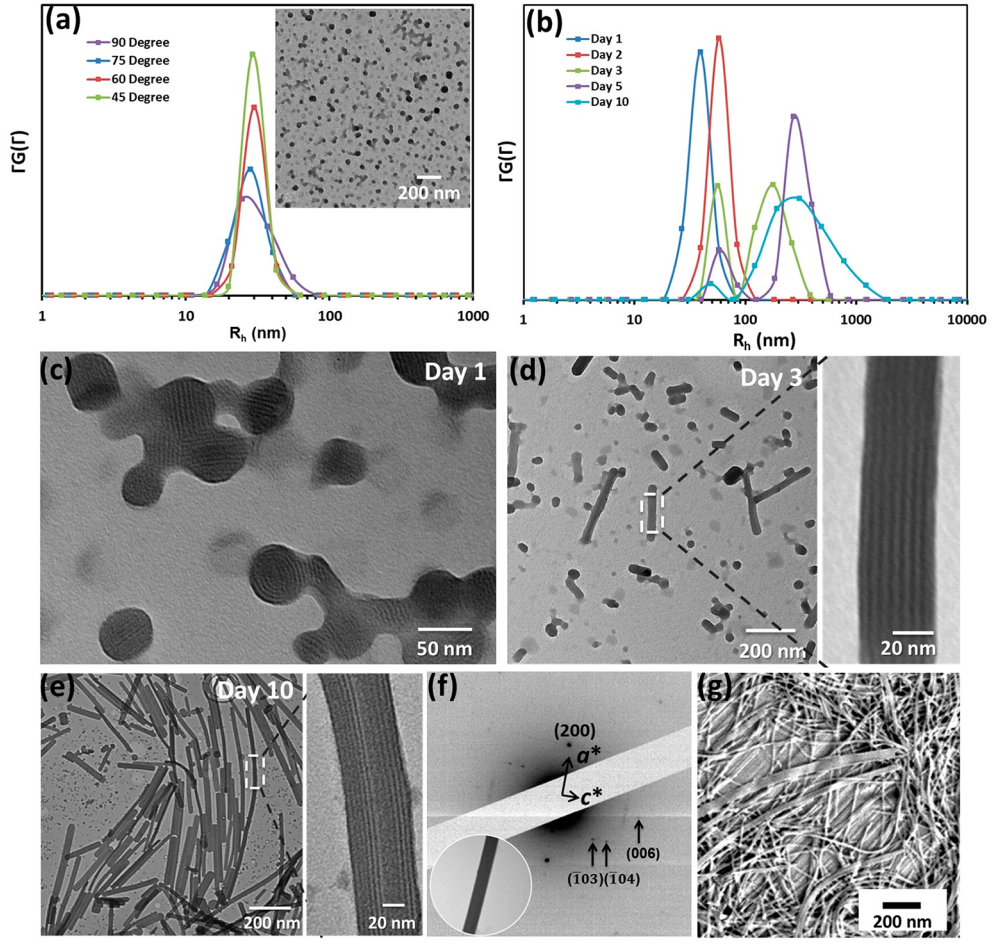

Figure 3. (a) Angle-variant DLS CONTIN analysis and corresponding TEM image (inset) of the self-assembled spheres of KPOM-BPOSS in solution at day 1. (b) Evolution of the DLS results within 10 days at a fixed detecting angle of 45°. (c) BF TEM image of the spherical aggregates with interior structures. (d,e) BF TEM images and amplified pictures of the nanobelts at day 3 and day 10, respectively. (f) SAED patterns of the circled individual nanobelt at the bottom left corner. (g) SEM image of the nanobelts formed at day 10.

Michael addition" reaction[67] between thiol groups and maleimidyl groups, which has been widely used for modular syntheses of hybrid materials and modifications of biomacromolecules with high efficiency under mild reaction conditions,[68] was used to prepare KPOM-2BPOSS (Scheme 1c). Comparison of the self-assembly behaviors from these three MJPs will provide insights into the effects of the relative volume fraction and interactions on their supramolecular structures.

The successful conjugation of KPOM-BPOSS, KPOM-CPOSS, and KPOM-2BPOSS has been evidenced in FT-IR, ^{1}H NMR, ^{13}C NMR (see Figures S1−S5 in the Supporting Information, SI), ^{31}P NMR spectra (Figure 1a), and MALDI-TOF mass spectra (Figure 1b). In particular, since ^{31}P NMR is highly sensitive to detect differences in chemical structures of the ligands attached on POM derivatives,[69] the observed single ^{31}P resonance peaks in Figure 1a indicate precisely defined chemical structures and high purity of the MJP samples. Moreover, in the MALDI-TOF mass spectra shown in Figure 1b, sharp single peaks corresponding to ionized MJP molecules with one additional captured tetrabutylammonium (TBA) cation are observed, which agree well with the calculated m/z values from their proposed chemical compositions. Detailed synthetic procedures and characterization results of these samples can be found in the SI.

3D Lamellar and 1D Nanobelt Crystals of KPOM-BPOSS in Solution with Different Solvent Polarity. Considering the solubility of KPOM-BPOSS in common organic solvents, we first studied its self-assembly in solvents with moderate polarity. Chloroform (ε = 4.8 at room temperature) vapor was allowed to slowly diffuse into a methanol (ε = 33) solution of KPOM-BPOSS (0.5 wt %) until the solution became turbid, forming white precipitates. Powder samples of KPOM-BPOSS were collected *via* high-speed centrifuge. Combined small-angle X-ray scattering (SAXS) and wide-angle X-ray diffraction (WAXD) patterns of this sample (Figure 2a) show three strong diffraction peaks in the low scattering angle range with a q ratio of 1:2:3, and the corresponding d-spacing values are 4.06, 2.03, and 1.35 nm. Observation of multiple diffraction peaks in the WAXD pattern suggests that this sample is highly crystalline.

Single crystals grown for microscopic experiments were carried out *via* slow diffusion of chloroform vapor into a small droplet of 0.5 wt % methanol solution of KPOM-BPOSS on carbon-coated mica. Multiple-layered lamellae are observed under an atomic force microscope (AFM) in Figure 2b and bright-field (BF) transmission electron microscopy (TEM) in Figure 2c. Statistical height measurements by AFM give rise to an average thickness of 4.1 ± 0.2 nm for a single layer of the stacked lamellae, which matches the d-spacing of the first

DOI: 10.1021/acsnano.6b01336
ACS Nano 2016, 10, 6585−6596

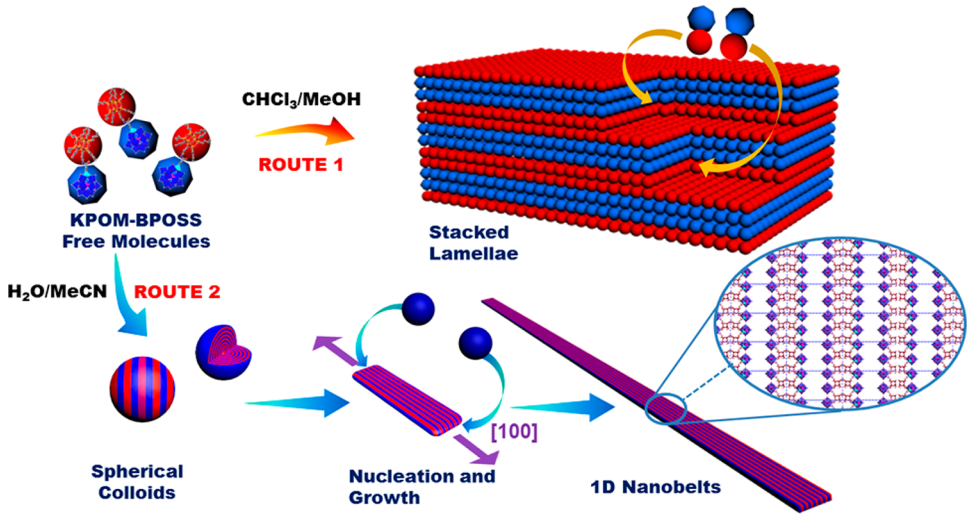

Figure 4. Cartoon illustration of the proposed mechanisms of forming the stacked lamellae in chloroform/methanol and the 1D nanobelts in water/acetonitrile.

diffraction peak in the SAXS pattern of the KPOM-BPOSS powder crystals. Furthermore, selected area electron diffraction (SAED) patterns in Figure 2d indicate that the multiple-layered lamellae in Figure 2c possess the same crystal lattice registration. The results of tilted SAED experiments are shown in Figure S6. Based on these SAED experiments, the crystal structure of KPOM-BPOSS was determined to be an orthorhombic unit cell with dimensions of a = 2.68 nm, b = 1.38 nm, and c = 4.06 nm (for detailed structure determination, see SI). Density measurements provide a value of 2.02 ± 0.01 g/cm^3, matching well with the calculated density of 2.04 g/cm^3 using the determined unit cell dimensions and number of molecules in each unit cell (Z = 4).

Computer simulation of the crystal structure was carried out using the Accelrys Cerius^2 package with a universal force field. Considering the minor contribution of the TBA counterions to the diffraction patterns, they have been omitted in the computer simulation in order to focus on the molecular arrangement of KPOM-BPOSS MJPs. Based on the orthorhombic unit cell parameters and the systematic extinction at (hk0), where h + k is odd (Figure 2d), a molecular packing model with a C211 space group has been built. The calculated single-crystal electron diffraction patterns of the [001] zone are presented in Figure 2e. They were in good agreement with the experimental SAED patterns in Figure 2d. A 3D view of a 3 × 3 × 2 crystal lattice is shown in Figure 2f, as well as the projections of this simulated crystal lattice on bc-, ca-, and ab-planes. The bc-plane and ac-plane projections reveal the head-to-head packing of the both MNPs along the c-axis, resulting in an alternative double-layered lamellae structure. It should be noted that this molecular packing leaves a lot of packing space for the BPOSS cages. Based on the pristine BPOSS crystals with a triclinic lattice,[70] an individual BPOSS cage occupies a volume of 1.2 nm^3, while in this KPOM-BPOSS crystal, the estimated volume for each BPOSS cage is ∼2.5 nm^3. We can thus deduce that it is the interactions of the Keggin POM clusters rather than those of the BPOSS cages that drive the crystal formation of KPOM-BPOSS.

To initiate self-assembled structures in solution with high solvent polarity, distilled water (ε = 80) was slowly added into a 0.1 wt % acetonitrile (ε = 37.5) solution of KPOM-BPOSS at a rate of 50 μL/h until reaching a final water volume fraction ($v_f^{H_2O}$) of 90%. Dynamic light scattering (DLS) experiments were carried out to simultaneously monitor the structural formation processes in solution. The observed DLS intensity is relatively low (<100 kcps) until $v_f^{H_2O}$ reached 20%. Beyond this point, the DLS intensity starts to increase while the solution still remains optically transparent (Figure S7). The maximum DLS intensity is observed at $v_f^{H_2O}$ = 70%, after which the solution becomes opaque. Obvious precipitation takes place when $v_f^{H_2O}$ = 90% is reached. Based on this observation, we have decided to keep the solution at $v_f^{H_2O}$ = 70% under iso-concentration conditions to study the structural evolution of KPOM-BPOSS assemblies as a function of time.

One day after adding water to $v_f^{H_2O}$ = 70%, CONTIN analysis of the DLS data collected at different scattering angles (45, 60, 75, and 90°) shows the formation of self-assembled nanostructures with an average hydrodynamic radius (R_h) of 30 ± 2 nm, which is independent of the detecting angles. The angular independence of the R_h value indicates the formation of colloidal spheres, which is also confirmed by the BF TEM image (inset of Figure 3a). Interestingly, in most cases, the internal structures of these spheres are visualized as lamellar structures, most of which are flat, while others are curved in side views (Figure 3c). Other minor internal structures can also be observed, which are judged to be intermediate states during the lamellar formation. SAED experiments on the colloidal particles show no diffraction spots, indicating that no crystals are formed within these colloidal spheres.

The formation of self-assembled nanostructures was continuously monitored for a few more days by DLS while keeping the solution steady and undisturbed (Figure 3b). At day 2, the average R_h value deduced from DLS data increases to 60 nm (red line in Figure 3b). An extra distribution peak corresponding to a larger R_h value (∼200 nm, green line in Figure 3b) is observed in the CONTIN analysis at day 3, along with decreased probability of the first peak, with an R_h value of 60 nm. At the same time, some elongated nanobelt structure starts to develop, as revealed in the BF TEM image (Figure 3d). A zoomed-in image shows that the elongated nanobelt structures possess an internal lamellar structure with a periodicity of *ca.* 4 nm. At day 5, the partition difference between the two peaks becomes more prominent (purple line in Figure 3b). Moreover, the peak centered at a larger R_h value

DOI: 10.1021/acsnano.6b01336
ACS Nano 2016, 10, 6585−6596

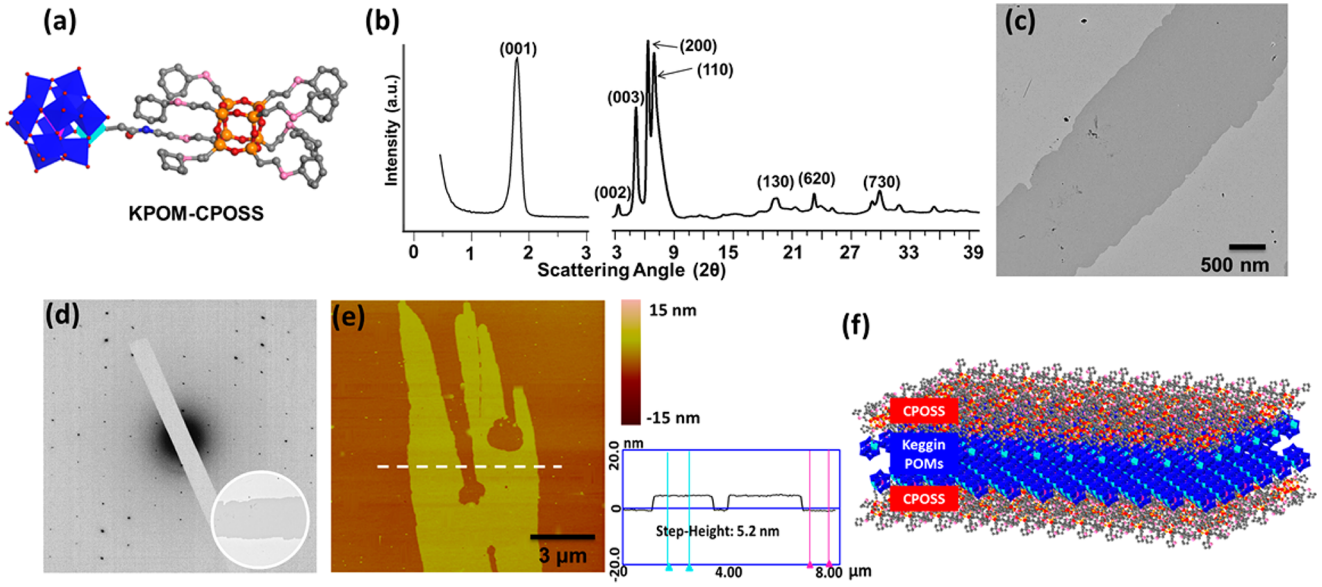

Figure 5. (a) Chemical structure model of KPOM-CPOSS. (b) SAXS and WAXD patterns of the powder crystals of KPOM-CPOSS. (c) BF TEM image of the 2D nanosheet morphology of KPOM-CPOSS. (d) SAED patterns from the 2D nanocrystal shown in the inset. (e) AFM height measurement of the 2D nanocrystal. (f) Schematic representation of the structure configuration of the 2D nanocrystal.

exhibits apparent scattering angular dependence, further revealing that the objects represented by this peak are no longer spherical. After standing for 10 days, a large number of extended nanobelts with internal lamellar crystals are observed (Figure 3e). The nanobelt morphology is also confirmed by a scanning electron microscopy (SEM) image (Figure 3g), revealing the considerable shape anisotropy between the width/thickness and the length of the nanobelt crystals. A SAED pattern of a single nanobelt displays a pair of strong diffraction spots along the extended direction, with corresponding *d*-spacing of 1.31 nm, and a few weaker spots in the quadrants (Figure 3f). Comparing this SAED pattern with that from the single crystal (Figure 2d), we could index this pair of strong spots to be (200), and thus, the elongated direction of the 1D nanobelt crystals is thus determined to be parallel to the *a*-axis of the orthorhombic lattice. Although rather weak, the diffraction spots in the quadrants could also be indexed as $(\bar{1}03)$ and $(\bar{1}04)$. Therefore, the SAED pattern in Figure 3f is along the [010] zone.

The distinct crystal morphologies of KPOM-BPOSS observed in different solutions suggest strong solvent polarity dependence. As illustrated in Figure 4, when dissolved in either methanol or acetonitrile, the resulting KPOM-BPOSS solutions contained no assemblies, as confirmed by DLS, indicating they are genuine solutions. Following route 1, when chloroform vapor slowly diffuses into the KPOM-BPOSS/methanol solution, the solubility of the POM cluster gradually decreases, which drives KPOM-BPOSS molecules to assemble *via* crystallization of Keggin subunits, resulting in the formation of the stacked lamellae (Figure 2b,c). Crystallization of both Keggin POM and BPOSS clusters shows the flat interface in the 3D crystal structures.

In route 2, however, adding water into the KPOM-BPOSS/acetonitrile solution leads to a sudden drop in solubility of both subunits. As a result, self-assembly *via* kinetically favorable pathways dominates to form metastable spherical colloids.[71] The internal lamellar structures within the colloidal spheres (Figure 3b) result from nanophase separation of the KPOM and BPOSS clusters, yet no crystallization process takes place. In a recent report, Ma *et al.* studied the formation of filled honeycomb structures of a Wells−Dawson-type POM-BPOSS MJP in acetonitrile/water mixtures.[57] Stabilization of the hexagonal close-packed cylinders is attributed to the proper size asymmetry of the Wells−Dawson-type POM and BPOSS clusters based on computer simulation results.[57] In our case, the size asymmetry of Keggin POM and BPOSS clusters is not big enough to stabilize the hexagonal packing. Instead, nanophase separation thus leads to the formation of an internal lamellar structure in the colloidal spheres.

We further reason that the internal lamellar structures in the colloidal spheres still possess higher free energy due to the amorphous nature compared to the flat lamellae crystals in 1D nanobelts. This provides the thermodynamic driving force for the morphological evolution. As indicated by our DLS results (Figure 3b), growth of the 1D nanobelt crystals is kinetically much slower. At day 3, short nanobelt crystals are found to coexist with the colloidal spheres (Figure 3d), while at day 10, nanobelt crystals are the dominant structures with increased lengths up to >1 μm (Figure 3e). As schematically illustrated in Figure 4, the proposed formation mechanism of the nanobelt crystals is *via* the nucleation and growth pathway, with a preferred crystal growth along the [100] direction to result in the high geometric anisotropy of 1D nanobelt crystals.

2D Nanosheets and Spherical Aggregates of KPOM-CPOSS in Solution with Different Solvent Polarity. We have shown two structural formation pathways of KPOM-BPOSS that are regulated by the solvent polarity. The structure analysis reveals that Keggin POM clusters dominate, in both cases, the molecular packing in the crystal lattice. Although the packing of BPOSS cages within the lamellar structure of KPOM-BPOSS (Figure 2c) differs from the favorable packing scheme found in its own crystal structure, the regular crystalline interlayer registration of those neighboring lamellae indicates that BPOSS cages indeed assist maintaining the crystallographic lattice in the lamellar normal direction. We, thus, speculate that the crystalline nature of BPOSS cages may inevitably play a

DOI: 10.1021/acsnano.6b01336
ACS Nano 2016, 10, 6585−6596

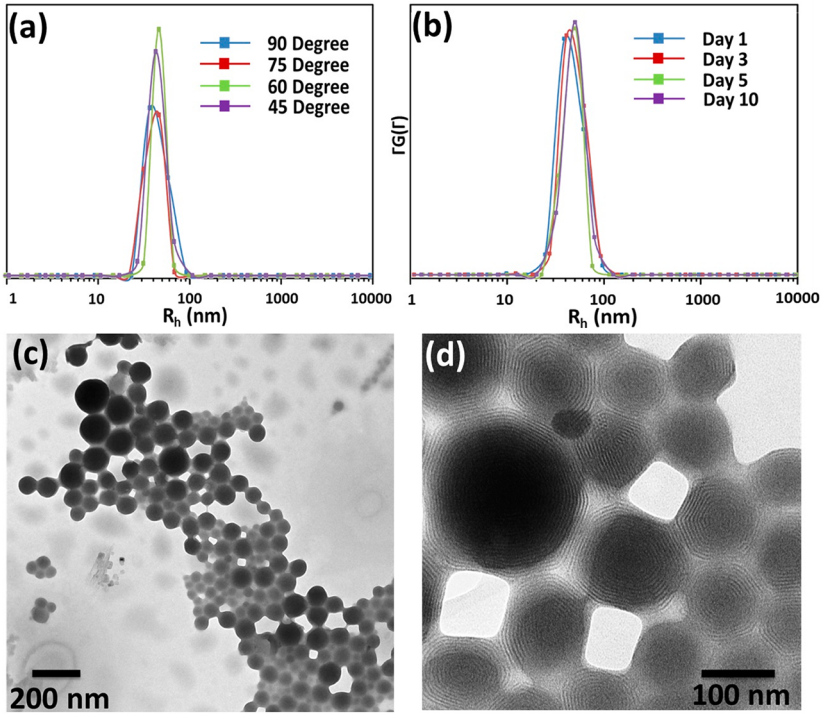

Figure 6. (a) Angle-variant DLS CONTIN analysis of the self-assembled spheres of KPOM-CPOSS in acetonitrile/water solution at day 1. (b) DLS results within 10 days collected at the fixed detecting angle of 45°. (c,d) BF TEM images of the spherical aggregates with curved lamella internal structures.

critical role in the morphological change observed in the acetonitrile/water solution of KPOM-BPOSS.

To verify these speculations, another conjugate, KPOM-CPOSS, composed of a Keggin POM with a cyclohexyl-substituted POSS derivative (CPOSS, Figure 5a), was prepared following the same procedure as that with KPOM-BPOSS (Scheme 1b; see synthetic details in theSI). In contrast to BPOSS derivatives, the CPOSS-NH_2 precursor is a viscous liquid at ambient temperature. By replacing the crystallizable BPOSS with the amorphous CPOSS, we are able to unambiguously isolate and study the influence of secondary interactions of the POSS cages on the structural formation of these two MJPs.

The powder polycrystals of KPOM-CPOSS were prepared similarly by slow diffusion of chloroform vapor into its methanol solution (0.5 wt %). Figure 5b shows the combined SAXS and WAXD patterns of KPOM-CPOSS polycrystals. Compared to the patterns of KPOM-BPOSS shown in Figure 2a, in the high scattering angle region ($2\theta > 6°$), the diffraction patterns of the two samples are almost identical. Based on the crystal parameters of KPOM-BPOSS, the WAXD patterns are indexed accordingly. As a result, the diffraction peaks at the high angle region must be attributed to the crystalline Keggin POM layers. The three strong diffraction peaks in the low scattering angle region ($2\theta < 6°$) with a q ratio of 1:2:3 also indicate a layered structure. However, the corresponding d-spacing value of the first peak is 4.99 nm, larger than that of the KPOM-BPOSS crystals (4.06 nm). The increased lamellar periodicity in KPOM-CPOSS may be attributed to the bigger size of the cyclohexyl groups compared to the size of isobutyl groups in KPOM-BPOSS. Moreover, the increased size of CPOSS also leads to a size asymmetry for KPOM-CPOSS smaller than that of KPOM-BPOSS, which further favors the formation of lamellae in the self-assembled structures.

In great contrast to the stacked lamellar single crystals of KPOM-BPOSS from chloroform/methanol solution, single crystals of KPOM-CPOSS showing 2D nanosheet morphology can be obtained by slow diffusion of chloroform vapor into the methanol solutions of KPOM-CPOSS with different molecular concentrations (0.1 to 0.5 wt %), as revealed by BF TEM images (*e.g.*, Figure 5c). The average height of these 2D nanosheets is measured by AFM to be 5.1 ± 0.2 nm (Figure 5e), which is close to the d-spacing of the first peak in the SAXS pattern (Figure 5b). SAED experiments (Figure 5d) confirm that the 2D KPOM-CPOSS nanocrystal does possess the same ED pattern as the [001] zone pattern of KPOM-BPOSS (Figure 2d). By purposely using KPOM-CPOSS solutions with higher initial concentrations (1.0 wt %), multilayered crystals can be observed (Figure S8a). However, in contrast to the SAED patterns of KPOM-BPOSS stacked lamellar crystals, SAED patterns of the overlapped crystals do not display crystallographic lattice registration along the lamellar normal direction (Figure S8b). Based on the diffraction data and thickness measurements, it can be concluded that the 2D nanosheet crystals of KPOM-CPOSS consist of two internal layers of crystalline Keggin POMs covered by two layers of amorphous CPOSS cages, as schematically illustrated in Figure 5f. Yet, due to the amorphous nature, the CPOSS cages do not possess crystallographic registration when multiple 2D nanocrystals stack along the normal direction of the nanosheets, thus preventing the formation of bulk single crystals with crystallographic registration along the lamellar normal direction.

The noncrystalline nature of CPOSS cages also results in different self-assembly behaviors of KPOM-CPOSS in the acetonitrile/water solution. When distilled water is slowly added into its 0.1 wt % acetonitrile solution, spherical aggregates are detected by DLS measurements at different detecting angles (Figure 6a). However, even after prolonged

DOI: 10.1021/acsnano.6b01336
ACS Nano 2016, 10, 6585−6596

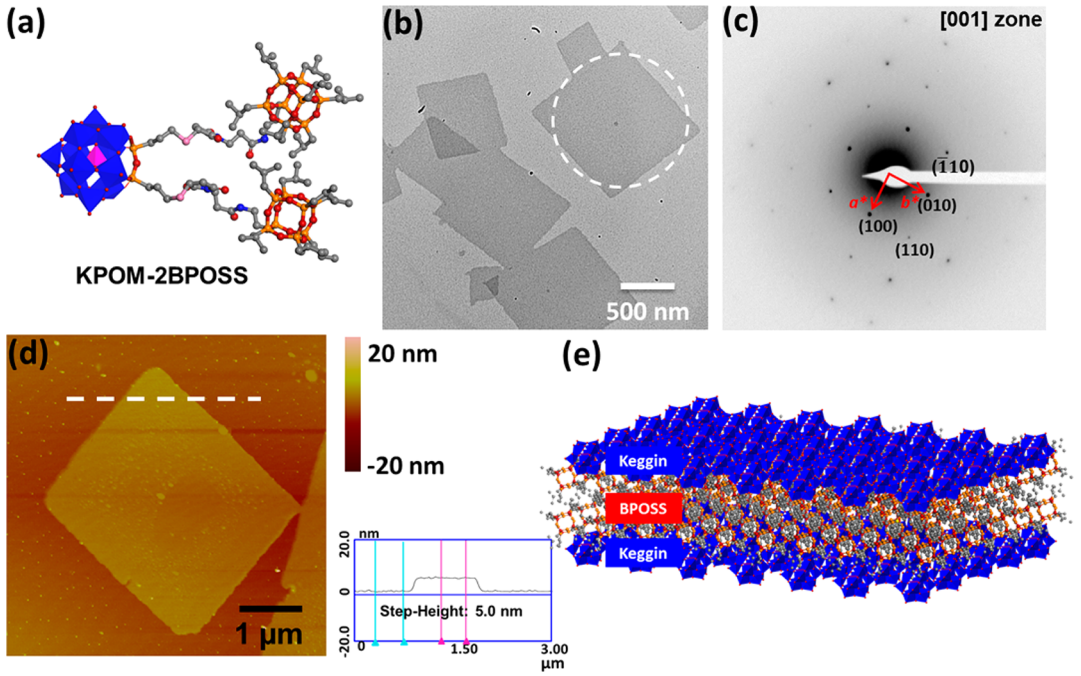

Figure 7. (a) Chemical structure model of KPOM-2BPOSS. (b) BF TEM image of the 2D nanosheets of KPOM-2BPOSS. (c) SAED patterns of the selected single crystal in (b). (d) AFM height measurement of a single nanosheet. (e) Schematic representation of the structure configuration of the 2D nanosheet.

aging for 10 days, no further structural evolution was observed for KPOM-CPOSS. The CONTIN analysis of the DLS data still shows spherical aggregates with a slightly increased R_h at day 10 (Figure 6b). The spherical aggregates are visualized by BF TEM images (Figure 6c). A zoomed-in image clearly shows their internal curved lamellar structures formed by nanophase separation (Figure 6d), similar to those observed in the case of KPOM-BPOSS under identical conditions. Therefore, it can be deduced that the crystallizable BPOSS cages are a crucial factor to facilitate the morphological evolution from colloidal nanoparticles to 1D nanobelt crystals in the KPOM-BPOSS sample in polar solvents.

It is also worth noting that the comparison between KPOM-BPOSS and KPOM-CPOSS reflects the combined effects of both size and polarity (interactions) of the periphery functional groups on the POSS cages. To further isolate these two factors, in future studies, it would be scientifically intriguing to replace the alkyl chains of both samples with their fluorinated counterparts that have almost identical sizes but different polarity.

Formation of BPOSS-Dominated 2D Nanosheets by Doubling the Number of BPOSS Cages. In the case of KPOM-BPOSS, the Keggin POMs play the leading role in the self-assembly process, due mainly to the larger size of the Keggin POM cluster compared to that of the BPOSS cage. Because the crystallization of Keggin POMs is highly impacted by the polarity of the solvents, distinct self-assembled structures were observed in different solvent mixtures. By doubling the number of BPOSS cages that are covalently linked to the Keggin POM, it is possible to switch the roles of the two MNPs in dictating crystal packing of the resulting MJPs. Moreover, we expect that when the BPOSS cages become the dominating building blocks, self-assembly of KPOM-2BPOSS could show weaker solvent polarity dependence because the crystallization of hydrophobic BPOSS cages may be less sensitive to the solvent polarity. It is also worth noting that the conjugate KPOM-2BPOSS is actually an ABA triad molecule, which should be termed as a "triblock" MJP.[72] For purposes of simplicity, however, KPOM-2BPOSS will be viewed as one special kind of MJP throughout this contribution.

To prove this, we designed and prepared a KPOM-2BPOSS "triblock" MJP through the thiol−Michael addition reaction (Scheme 1c and Figure 7a). Polycrystals (for X-ray experiments) and single crystals (for TEM experiments) of KPOM-2BPOSS were grown by slow diffusion of methanol vapor into its chloroform solution. From the combined SAXS and WAXD patterns shown in Figure S9, we deduced a layered structure with crystalline packing within the layers. The *d*-spacing of the first peak is calculated to be 4.7 nm. More importantly, the diffraction peaks at the high angle region are completely different from those observed in the cases of KPOM-BPOSS (Figure 2a) and KPOM-CPOSS (Figure 5b). In Figure 7b, the bright-field TEM image exhibits 2D rhombic nanosheet morphology with a lateral size of several micrometers. The SAED patterns of KPOM-2BPOSS single crystals in Figure 7c are again different from those of the stacked lamellar crystals of KPOM-BPOSS (Figure 2c) and the 2D nanosheets of KPOM-CPOSS (Figure 5d) but are identical to the [001] zone electron diffractions of the BPOSS single crystal (a triclinic unit cell with a = 1.04 nm, b = 0.97 nm, c = 1.16 nm, α = 74.5°, β = 82.0°, γ = 80.0°, and a *P*1 space group).[70] The crystal structure of KPOM-2BPOSS is thus dominantly formed *via* the BPOSS cages. The AFM height analysis of the 2D nanocrystals gives a statistic thickness of 5.0 ± 0.2 nm (Figure 7d), which fits well with the *d*-spacing of the first diffraction peak in the SAXS data. The crystal structure of KPOM-2BPOSS can thus be depicted based on the molecular packing of BPOSS single crystals, which are sandwiched by two outer POM layers (Figure 7e). Notably, 2D nanosheets with the same molecular packing can also be obtained by adding water into the acetone or DMF solutions of

DOI: 10.1021/acsnano.6b01336
ACS Nano 2016, 10, 6585−6596

KPOM-2BPOSS (Figure S10), confirming the insensitivity to solvent polarity of this self-assembled structure.[70]

In analogy to previously reported MJPs,[42] the formation of 2D nanocrystals of KPOM-2BPOSS can be explained by a similar mechanism. KPOM-2BPOSS is well-dissolved in chloroform as a true solution, while methanol is a moderate solvent for Keggin POMs but a poor solvent for BPOSS cages. Upon diffusion of methanol vapor into the chloroform solution, the solubility of KPOM-2BPOSS in the mixed solution gradually decreases, and the secondary interactions among the BPOSS cages drive the formation of a crystalline BPOSS bilayer (Figure 7e), while the counterions of Keggin POM clusters are still solvated in solution, resulting in the net negative charges on the surface of 2D nanosheets. The electrostatic repulsive interactions prevent the contact of two single sheets and, therefore, stabilize the independent 2D nanosheet crystals. Different from the definite molecular packing arrangement of POMs in the crystals of KPOM-BPOSS, the Keggin clusters lack both the transitional and orientational symmetry on the surface of the 2D nanosheets of KPOM-2BPOSS, which is evidenced by failure to observe diffractions associated with the Keggin POM crystal structure in the SAED patterns (Figure 7c). Formation of 2D nanosheet crystals from KPOM-2BPOSS also indicates the dominant role of BPOSS cage crystallization to result in structures with flat interfaces.[47]

CONCLUSION

In summary, three sets of amphiphilic MJPs (KPOM-BPOSS, KPOM-CPOSS, and KPOM-2BPOSS) have been rationally designed and synthesized to study the effects of different types of secondary interactions on manipulating the dimensions of their self-assembled nanostructures. For KPOM-BPOSS, the Keggin POM clusters play the leading role in the self-assembly process due to a larger molecular size. Since a Keggin POM is composed of a negatively charged cluster and several positive TBA counterions, electrostatic interactions among KPOM-BPOSS are strongly influenced by the solvent polarity. In a highly polar solvent mixture of acetonitrile/water, a morphological transition from colloidal spheres with internal lamellar structures (formed due to nanophase separation) to 1D nanobelt crystals was observed, whereas in a moderately polar solvent mixture of chloroform/methanol, multiple-layered stacked single crystals of KPOM-BPOSS were obtained. The role of interactions among BPOSS cages in this transition process can be illustrated by comparing the assembling structures of KPOM-BPOSS with KPOM-CPOSS under similar conditions. In the acetonitrile/water mixture, colloidal spheres of KPOM-CPOSS with inner curved lamellar structures are also found. However, no further morphology transition toward 1D nanobelt crystals takes place during the aging. In the chloroform/methanol mixture, KPOM-CPOSS can self-assemble into 2D nanosheets with a uniform thickness. SAED patterns reveal that those 2D nanosheets can be depicted as a crystalline Keggin POM bilayer sandwiched by two single layers of outlying CPOSS cages. These results suggest that although the crystal structures of KPOM-BPOSS/CPOSS are dominated by Keggin POMs, the crystal dimensions can be manipulated by tuning the secondary interactions among the functionalized POSS cages. When the number of BPOSS cages tethered to a Keggin POM cluster is doubled, the BPOSS cages became the structure-determining MNP subunits in KPOM-2BPOSS. The self-assembled structures of KPOM-2BPOSS showed no strong dependence on solvent polarity. In various solvent mixtures, essentially identical 2D nanosheet morphology was observed for KPOM-2BPOSS. Furthermore, the KPOM-2BPOSS nanosheets possess an inverse structure configuration, which is composed of a crystalline BPOSS bilayer sandwiched by two layers of Keggin POM clusters. A different structure formation mechanism is proposed for KPOM-2BPOSS, which emphasizes crystallization of BPOSS cages as the driving force, due to the larger geometric size and crystallization ability. Repulsive electrostatic interactions of the outlying POM clusters suppress the crystal growth along the normal direction. This study presents a strategy to manipulate dimensions and structures of supramolecular assembles of MJPs *via* rational molecular design and fine-tuning of the secondary interactions among the MNP subunits and, thus, provides a prototype to direct the molecular packing and locations of functional nanoparticles of supramolecular assembled structures for potential applications. In particular, MJPs based on various POM building blocks could be potentially useful in applications related to the POM clusters, which range from catalysis,[73] electrochemistry,[74] photochromism,[75] magnetism,[76] to medicine.[77]

METHODS

SAXS. SAXS experiments were performed on a Rigaku MicroMax 003+ instrument equipped with a 2D Pilatus 200 K silicon detector. The working voltage and current for the X-ray tube were 50 kV and 0.6 mA, respectively. The wavelength of the X-ray was 0.154 nm. The scattering vector (q) was calibrated using silver behenate with the primary reflection peak at q = 1.067 nm^{-1}. The SAXS diffraction patterns covering the q range between 0.2 and 3.0 nm^{-1} were recorded. The background scattering was subtracted and further analyzed with the Rigaku software SAXSgui.

WAXD. WAXD experiments were conducted on the Rigaku Rapid II instrument equipped with a 12 kW (30 mA, 40 kV) rotating anode generator and an image plate as the detector. The instrument was calibrated using silicon powders with 2θ being 28.4° under Cu Kα radiation. The air and Kapton tape background scattering were subtracted. The 1D WAXD curve was integrated from the 2D image.

Electron Microscopy. TEM experiments were carried out with a Philips Tecnai 12 or a JEOL-1230 microscope with an accelerating voltage of 120 kV to record the bright-field images. TEM images were taken on a digital CCD camera and processed with the accessory digital imaging software. SAED patterns were obtained by using a tilting stage to determine the crystal structure parameters. The d-spacings were calibrated using an Al standard. SEM images were recorded using a JEOL JSM5310 microscope.

AFM. AFM experiments were performed on a Veeco Dimension ICON instrument to examine the sample morphology on the carbon-coated mica substrate by deposition from the corresponding solutions. The images were taken in the tapping mode. The scanning rate was set at 0.99 Hz for low-magnification images at a resolution of 512 × 512 pixels per image. Image modification was carried out by the NanoScope Anylysis 1.5 software.

Molecular Modeling. Molecular modeling and analysis of the diffraction patterns were performed using the Accelrys Cerius^2 software package. Basic unit cell parameters determined by crystallographic experimental data from combined SAXS, WAXD, and SAED experiments were used to build the crystal unit cell. The positions of atoms in this unit cell were judged by comparing their calculated diffraction patterns with experimental patterns.

DLS. DLS experiments were conducted on a Brookhaven Instruments Inc. light scattering spectrometer, equipped with a diode-pumped solid-state laser operating at 532 nm and a BI-9000AT multichannel digital correlator. The intensity−intensity time correlation functions were analyzed by the constrained regularized CONTIN method. The average apparent translational diffusion coefficient, D_{app}, was determined from the normalized distribution

DOI: 10.1021/acsnano.6b01336
ACS Nano 2016, 10, 6585−6596

function of the characteristic line width, $\Gamma(G)$. The hydrodynamic radius (R_h) was converted from D through the Stokes–Einstein equation: $R_h = kT/6\pi\eta D$, where k is the Boltzmann constant and η is the viscosity of the solvent at temperature T.

Sample Preparation. Powder crystals of KPOM-BPOSS and KPOM-CPOSS for X-ray measurements were grown *via* slow diffusion of chloroform vapor into their methanol solutions with an initial concentration of 0.5 wt % in a sealed chamber. During this time, the clear methanol solutions started to turn turbid and white flakes formed gradually. The solids were collected through high-speed centrifuge, dried *in vacuo*, and directly used to record the SAXS and WAXD data. Stacked lamellar samples of KPOM-BPOSS for TEM experiments were grown *via* slow diffusion of chloroform vapor into a small droplet of 0.5 wt % methanol solution of KPOM-BPOSS on carbon-coated mica. Then, the carbon film was separated from the mica substrate by carefully diffusing water into the carbon–mica interface. The floating carbon film was then picked up by copper grids for TEM experiments. Isolated 2D nanosheets of KPOM-CPOSS for TEM experiments were prepared following a similar procedure, with initial solution concentrations varied from 0.1 to 0.5 wt %. Samples for AFM measurements were prepared similarly on carbon-coated mica.

Powder crystals of KPOM-2BPOSS for X-ray measurements were obtained by slow diffusion of methanol vapor into its 0.5 wt % chloroform solution in a sealed chamber. The white crystals were collected through high-speed centrifuge, dried *in vacuo*, and directly used for the X-ray tests. Isolated 2D nanosheets of KPOM-2BPOSS for TEM experiments were grown by two methods: (1) slow diffusion of methanol vapor into its 0.5 wt % chloroform solution until the solution became turbid and (2) slow addition of water into 0.5 wt % DMF or acetone solutions of KPOM-2BPOSS until $v_f^{H_2O}$ = 20% was reached. Then, a small droplet of the resulting solutions was placed onto a carbon-coated copper grid, which was dried in air for the TEM experiments. A similar procedure was followed to prepare the AFM samples on carbon-coated mica.

ASSOCIATED CONTENT

Supporting Information

The Supporting Information is available free of charge on the ACS Publications website at DOI: 10.1021/acsnano.6b01336.

Details of the synthesis, chemical structure characterization, additional results and discussion (PDF)

AUTHOR INFORMATION

Corresponding Authors

*E-mail: tliu@uakron.edu.
*E-mail: ky13@zips.uakron.edu.
*E-mail: scheng@uakron.edu.

Notes

The authors declare no competing financial interest.

ACKNOWLEDGMENTS

This work was supported by National Science Foundation grant (DMR-1408872). The authors also thank K. Guo, Z. Guo, and C. Wesdemiotis at the University of Akron for assistance with the MALDI-TOF mass spectrometry.

REFERENCES

(1) Lehn, J.-M. Supramolecular Chemistry-Scope and Perspectives Molecules, Supermolecules, and Molecular Devices (Nobel Lecture). *Angew. Chem., Int. Ed. Engl.* **1988**, *27*, 89–112.

(2) Lehn, J.-M. Supramolecular Chemistry. *Science* **1993**, *260*, 1762–1763.

(3) Hawker, C. J.; Wooley, K. L. The Convergence of Synthetic Organic and Polymer Chemistries. *Science* **2005**, *309*, 1200–1205.

(4) Whitesides, G. M.; Boncheva, M. Beyond Molecules: Self-Assembly of Mesoscopic and Macroscopic Components. *Proc. Natl. Acad. Sci. U. S. A.* **2002**, *99*, 4769–4774.

(5) Hartgerink, J. D.; Beniash, E.; Stupp, S. I. Self-Assembly and Mineralization of Peptide-Amphiphile Nanofibers. *Science* **2001**, *294*, 1684–1688.

(6) Hill, J. P.; Jin, W.; Kosaka, A.; Fukushima, T.; Ichihara, H.; Shimomura, T.; Ito, K.; Hashizume, T.; Ishii, N.; Aida, T. Self-Assembled Hexa-Peri-Hexabenzocoronene Graphitic Nanotube. *Science* **2004**, *304*, 1481–1483.

(7) Wang, D.; Kou, R.; Choi, D.; Yang, Z.; Nie, Z.; Li, J.; Saraf, L. V.; Hu, D.; Zhang, J.; Graff, G. L.; Liu, J.; Pope, M. A.; Aksay, I. A. Ternary Self-Assembly of Ordered Metal Oxide-Graphene Nanocomposites for Electrochemical Energy Storage. *ACS Nano* **2010**, *4*, 1587–1595.

(8) Vijayakumar, C.; Praveen, V. K.; Ajayaghosh, A. RGB Emission through Controlled Donor Self-Assembly and Modulation of Excitation Energy Transfer: A Novel Strategy to White-Light-Emitting Organogels. *Adv. Mater.* **2009**, *21*, 2059–2063.

(9) Fendler, J. H. Chemical Self-Assembly for Electronic Applications. *Chem. Mater.* **2001**, *13*, 3196–3210.

(10) Rao, S. G.; Huang, L.; Setyawan, W.; Hong, S. Nanotube Electronics: Large-Scale Assembly of Carbon Nanotubes. *Nature* **2003**, *425*, 36–37.

(11) Hu, B.; Wang, S.-B.; Wang, K.; Zhang, M.; Yu, S.-H. Microwave-Assisted Rapid Facile "Green" Synthesis of Uniform Silver Nanoparticles: Self-Assembly into Multilayered Films and Their Optical Properties. *J. Phys. Chem. C* **2008**, *112*, 11169–11174.

(12) Liu, X.; Jiang, M. Optical Switching of Self-Assembly: Micellization and Micelle-Hollow-Sphere Transition of Hydrogen-Bonded Polymers. *Angew. Chem., Int. Ed.* **2006**, *45*, 3846–3850.

(13) Perez, J. M.; Simeone, F. J.; Saeki, Y.; Josephson, L.; Weissleder, R. Viral-Induced Self-Assembly of Magnetic Nanoparticles Allows the Detection of Viral Particles in Biological Media. *J. Am. Chem. Soc.* **2003**, *125*, 10192–10193.

(14) Khaled, A.; Guo, S.; Li, F.; Guo, P. Controllable Self-Assembly of Nanoparticles for Specific Delivery of Multiple Therapeutic Molecules to Cancer Cells Using RNA Nanotechnology. *Nano Lett.* **2005**, *5*, 1797–1808.

(15) Liu, J.; Huang, W.; Pang, Y.; Huang, P.; Zhu, X.; Zhou, Y.; Yan, D. Molecular Self-Assembly of a Homopolymer: An Alternative to Fabricate Drug-Delivery Platforms for Cancer Therapy. *Angew. Chem., Int. Ed.* **2011**, *50*, 9162–9166.

(16) Moulton, B.; Zaworotko, M. J. From Molecules to Crystal Engineering: Supramolecular Isomerism and Polymorphism in Network Solids. *Chem. Rev.* **2001**, *101*, 1629–1658.

(17) Zhang, W. B.; Yu, X. F.; Wang, C. L.; Sun, H. J.; Hsieh, I. F.; Li, Y. W.; Dong, X. H.; Yue, K.; Van Horn, R.; Cheng, S. Z. D. Molecular Nanoparticles Are Unique Elements for Macromolecular Science: From "Nanoatoms" to Giant Molecules. *Macromolecules* **2014**, *47*, 1221–1239.

(18) Zhang, W.-B.; Cheng, S. D. Toward Rational and Modular Molecular Design in Soft Matter Engineering. *Chin. J. Polym. Sci.* **2015**, *33*, 797–814.

(19) Yu, X.; Li, Y.; Dong, X.-H.; Yue, K.; Lin, Z.; Feng, X.; Huang, M.; Zhang, W.-B.; Cheng, S. Z. D. Giant Surfactants Based on Molecular Nanoparticles: Precise Synthesis and Solution Self-Assembly. *J. Polym. Sci., Part B: Polym. Phys.* **2014**, *52*, 1309–1325.

(20) Boott, C. E.; Nazemi, A.; Manners, I. Synthetic Covalent and Non-Covalent 2D Materials. *Angew. Chem., Int. Ed.* **2015**, *54*, 13876–13894.

(21) Walther, A.; Müller, A. H. E. Janus Particles: Synthesis, Self-Assembly, Physical Properties, and Applications. *Chem. Rev.* **2013**, *113*, 5194–5261.

(22) de Gennes, P.-G. Soft Matter (Nobel Lecture). *Angew. Chem., Int. Ed. Engl.* **1992**, *31*, 842–845.

(23) Li, Y.; Zhang, W.-B.; Hsieh, I.-F.; Zhang, G.; Cao, Y.; Li, X.; Wesdemiotis, C.; Lotz, B.; Xiong, H.; Cheng, S. Z. Breaking Symmetry toward Nonspherical Janus Particles Based on Polyhedral Oligomeric

DOI: 10.1021/acsnano.6b01336
ACS Nano 2016, 10, 6585–6596

Silsesquioxanes: Molecular Design,"Click" Synthesis, and Hierarchical Structure. *J. Am. Chem. Soc.* **2011**, *133*, 10712−10715.
(24) Nie, Z.; Li, W.; Seo, M.; Xu, S.; Kumacheva, E. Janus and Ternary Particles Generated by Microfluidic Synthesis: Design, Synthesis, and Self-Assembly. *J. Am. Chem. Soc.* **2006**, *128*, 9408−9412.
(25) Nisisako, T.; Torii, T.; Takahashi, T.; Takizawa, Y. Synthesis of Monodisperse Bicolored Janus Particles with Electrical Anisotropy Using a Microfluidic Co-Flow System. *Adv. Mater.* **2006**, *18*, 1152−1156.
(26) Liu; Abetz, V.; Müller, A. H. E. Janus Cylinders. *Macromolecules* **2003**, *36*, 7894−7898.
(27) Walther, A.; Muller, A. H. E. Janus Particles. *Soft Matter* **2008**, *4*, 663−668.
(28) Jiang, S.; Chen, Q.; Tripathy, M.; Luijten, E.; Schweizer, K. S.; Granick, S. Janus Particle Synthesis and Assembly. *Adv. Mater.* **2010**, *22*, 1060−1071.
(29) Asakawa, H.; Tahara, S.; Nakamichi, M.; Takehara, K.; Ikeno, S.; Linder, M. B.; Haruyama, T. The Amphiphilic Protein HFBII as a Genetically Taggable Molecular Carrier for the Formation of a Self-Organized Functional Protein Layer on a Solid Surface. *Langmuir* **2009**, *25*, 8841−8844.
(30) Varjonen, S.; Laaksonen, P.; Paananen, A.; Valo, H.; Hähl, H.; Laaksonen, T.; Linder, M. B. Self-Assembly of Cellulose Nanofibrils by Genetically Engineered Fusion Proteins. *Soft Matter* **2011**, *7*, 2402−2411.
(31) Date, R. W.; Bruce, D. W. Shape Amphiphiles: Mixing Rods and Disks in Liquid Crystals. *J. Am. Chem. Soc.* **2003**, *125*, 9012−9013.
(32) Glotzer, S. C.; Horsch, M. A.; Iacovella, C. R.; Zhang, Z.; Chan, E. R.; Zhang, X. Self-Assembly of Anisotropic Tethered Nanoparticle Shape Amphiphiles. *Curr. Opin. Colloid Interface Sci.* **2005**, *10*, 287−295.
(33) Chen, Q.; Whitmer, J. K.; Jiang, S.; Bae, S. C.; Luijten, E.; Granick, S. Supracolloidal Reaction Kinetics of Janus Spheres. *Science* **2011**, *331*, 199−202.
(34) Hu, J.; Zhou, S.; Sun, Y.; Fang, X.; Wu, L. Fabrication, Properties and Applications of Janus Particles. *Chem. Soc. Rev.* **2012**, *41*, 4356−4378.
(35) Lin, M.-C.; Hsu, C.-H.; Sun, H.-J.; Wang, C.-L.; Zhang, W.-B.; Li, Y.; Chen, H.-L.; Cheng, S. Z. D. Crystal Structure and Molecular Packing of an Asymmetric Giant Amphiphile Constructed by One C_{60} and Two POSSs. *Polymer* **2014**, *55*, 4514−4520.
(36) Walther, A.; Drechsler, M.; Rosenfeldt, S.; Harnau, L.; Ballauff, M.; Abetz, V.; Müller, A. H. E. Self-Assembly of Janus Cylinders into Hierarchical Superstructures. *J. Am. Chem. Soc.* **2009**, *131*, 4720−4728.
(37) Walther, A.; Barner-Kowollik, C.; Müller, A. H. E. Mixed, Multicompartment, or Janus Micelles? A Systematic Study of Thermoresponsive Bis-Hydrophilic Block Terpolymers. *Langmuir* **2010**, *26*, 12237−12246.
(38) Nie, L.; Liu, S.; Shen, W.; Chen, D.; Jiang, M. One-Pot Synthesis of Amphiphilic Polymeric Janus Particles and Their Self-Assembly into Supermicelles with a Narrow Size Distribution. *Angew. Chem., Int. Ed.* **2007**, *46*, 6321−6324.
(39) Hu, S.-H.; Gao, X. Nanocomposites with Spatially Separated Functionalities for Combined Imaging and Magnetolytic Therapy. *J. Am. Chem. Soc.* **2010**, *132*, 7234−7237.
(40) Sun, H.-J.; Tu, Y.; Wang, C.-L.; Van Horn, R. M.; Tsai, C.-C.; Graham, M. J.; Sun, B.; Lotz, B.; Zhang, W.-B.; Cheng, S. Z. Hierarchical Structure and Polymorphism of a Sphere-Cubic Shape Amphiphile Based on a Polyhedral Oligomeric Silsesquioxane-[60] Fullerene Conjugate. *J. Mater. Chem.* **2011**, *21*, 14240−14247.
(41) Lin, Z. W.; Lu, P. T.; Hsu, C. H.; Yue, K.; Dong, X. H.; Liu, H.; Guo, K.; Wesdemiotis, C.; Zhang, W. B.; Yu, X. F.; Cheng, S. Z. D. Self-Assembly of Fullerene-Based Janus Particles in Solution: Effects of Molecular Architecture and Solvent. *Chem. - Eur. J.* **2014**, *20*, 11630−11635.
(42) Liu, H.; Hsu, C.-H.; Lin, Z.; Shan, W.; Wang, J.; Jiang, J.; Huang, M.; Lotz, B.; Yu, X.; Zhang, W.-B.; Yue, K.; Cheng, S. Z. D. Two-Dimensional Nanocrystals of Molecular Janus Particles. *J. Am. Chem. Soc.* **2014**, *136*, 10691−10699.
(43) Robinson, I. Coherent Diffraction: Giant Molecules or Tiny Crystals? *Nat. Mater.* **2008**, *7*, 275−276.
(44) Roy, X.; Lee, C.-H.; Crowther, A. C.; Schenck, C. L.; Besara, T.; Lalancette, R. A.; Siegrist, T.; Stephens, P. W.; Brus, L. E.; Kim, P.; Steigerwald, M. L.; Nuckolls, C. Nanoscale Atoms in Solid-State Chemistry. *Science* **2013**, *341*, 157−160.
(45) Cordes, D. B.; Lickiss, P. D.; Rataboul, F. Recent Developments in the Chemistry of Cubic Polyhedral Oligosilsesquioxanes. *Chem. Rev.* **2010**, *110*, 2081−2173.
(46) Li, G.; Wang, L.; Ni, H.; Pittman, C. U., Jr Polyhedral Oligomeric Silsesquioxane (POSS) Polymers and Copolymers: A Review. *J. Inorg. Organomet. Polym.* **2001**, *11*, 123−154.
(47) Huang, M.; Hsu, C.-H.; Wang, J.; Mei, S.; Dong, X.; Li, Y.; Li, M.; Liu, H.; Zhang, W.; Aida, T.; Zhang, W.-B.; Yue, K.; Cheng, S. Z. D. Selective Assemblies of Giant Tetrahedra *via* Precisely Controlled Positional Interactions. *Science* **2015**, *348*, 424−428.
(48) Cordes, D. B.; Lickiss, P. D. Preparation and Characterization of Polyhedral Oligosilsesquioxanes. In *Applications of Polyhedral Oligomeric Silsesquioxanes*; Hartmann-Thompson, C., Ed.; Springer: Dordrecht, The Netherlands, 2011; pp 47−133.
(49) Montellano López, A.; Mateo-Alonso, A.; Prato, M. Materials Chemistry of Fullerene C 60 Derivatives. *J. Mater. Chem.* **2011**, *21*, 1305−1318.
(50) Liu, T. Supramolecular Structures of Polyoxomolybdate-Based Giant Molecules in Aqueous Solution. *J. Am. Chem. Soc.* **2002**, *124*, 10942−10943.
(51) Li, D.; Yin, P.; Liu, T. Supramolecular Architectures Assembled from Amphiphilic Hybrid Polyoxometalates. *Dalton Trans.* **2012**, *41*, 2853−2861.
(52) Proust, A.; Matt, B.; Villanneau, R.; Guillemot, G.; Gouzerh, P.; Izzet, G. Functionalization and Post-Functionalization: A Step towards Polyoxometalate-Based Materials. *Chem. Soc. Rev.* **2012**, *41*, 7605−7622.
(53) Hou, Z.-Y.; Hu, M.; Wang, W. Synthesis and Self-Assembled Structure of a Cluster-Cluster Hybrid Molecule Composed of POM and POSS Clusters. *Huaxue Xuebao* **2014**, *72*, 61−68.
(54) Hu, M.-B.; Hou, Z.-Y.; Hao, W.-Q.; Xiao, Y.; Yu, W.; Ma, C.; Ren, L.-J.; Zheng, P.; Wang, W. POM-Organic-POSS Cocluster: Creating a Dumbbell-Shaped Hybrid Molecule for Programming Hierarchical Supramolecular Nanostructures. *Langmuir* **2013**, *29*, 5714−5722.
(55) Kang, H. J.; Paterson, N. G.; Gaspar, A. H.; Ton-That, H.; Baker, E. N. The Corynebacterium Diphtheriae Shaft Pilin SpaA Is Built of Tandem Ig-Like Modules with Stabilizing Isopeptide and Disulfide Bonds. *Proc. Natl. Acad. Sci. U. S. A.* **2009**, *106*, 16967−16971.
(56) Liljeström, V.; Mikkilä, J.; Kostiainen, M. A. Self-Assembly and Modular Functionalization of Three-Dimensional Crystals from Oppositely Charged Proteins. *Nat. Commun.* **2014**, *5*, 5445.
(57) Ma, C.; Wu, H.; Huang, Z.-H.; Guo, R.-H.; Hu, M.-B.; Kübel, C.; Yan, L.-T.; Wang, W. A Filled-Honeycomb-Structured Crystal Formed by Self-Assembly of a Janus Polyoxometalate-Silsesquioxane (POM-POSS) Co-Cluster. *Angew. Chem., Int. Ed.* **2015**, *54*, 15699−15704.
(58) Nisar, A.; Wang, X. Surfactant-Encapsulated Polyoxometalate Building Blocks: Controlled Assembly and Their Catalytic Properties. *Dalton Trans.* **2012**, *41*, 9832−9845.
(59) Zhang, J.; Song, Y.-F.; Cronin, L.; Liu, T. Self-Assembly of Organic-Inorganic Hybrid Amphiphilic Surfactants with Large Polyoxometalates as Polar Head Groups. *J. Am. Chem. Soc.* **2008**, *130*, 14408−14409.
(60) Li, D.; Song, J.; Yin, P.; Simotwo, S.; Bassler, A. J.; Aung, Y.; Roberts, J. E.; Hardcastle, K. I.; Hill, C. L.; Liu, T. Inorganic-Organic Hybrid Vesicles with Counterion- and pH-Controlled Fluorescent Properties. *J. Am. Chem. Soc.* **2011**, *133*, 14010−14016.

DOI: 10.1021/acsnano.6b01336
ACS Nano 2016, 10, 6585−6596

(61) Matt, B.; Renaudineau, S.; Chamoreau, L. M.; Afonso, C.; Izzet, G.; Proust, A. Hybrid Polyoxometalates: Keggin and Dawson Silyl Derivatives as Versatile Platforms. *J. Org. Chem.* **2011**, *76*, 3107−3112.
(62) Matt, B.; Moussa, J.; Chamoreau, L.-M.; Afonso, C.; Proust, A.; Amouri, H.; Izzet, G. Elegant Approach to the Synthesis of a Unique Heteroleptic Cyclometalated Iridium(III)-Polyoxometalate Conjugate. *Organometallics* **2012**, *31*, 35−38.
(63) Sazani, G.; Pope, M. T. Organotin and Organogermanium Linkers for Simple, Direct Functionalization of Polyoxotungstates. *Dalton Trans.* **2004**, 1989−1994.
(64) Aoki, S.; Kurashina, T.; Kasahara, Y.; Nishijima, T.; Nomiya, K. Polyoxometalate (POM)-Based, Multi-Functional, Inorganic-Organic, Hybrid Compounds: Syntheses and Molecular Structures of Silanol- and/or Siloxane Bond-Containing Species Grafted on Mono- and Tri-Lacunary Keggin POMs. *Dalton Trans.* **2011**, *40*, 1243−1253.
(65) Micoine, K.; Hasenknopf, B.; Thorimbert, S.; Lacôte, E.; Malacria, M. A General Strategy for Ligation of Organic and Biological Molecules to Dawson and Keggin Polyoxotungstates. *Org. Lett.* **2007**, *9*, 3981−3984.
(66) Bareyt, S.; Piligkos, S.; Hasenknopf, B.; Gouzerh, P.; Lacôte, E.; Thorimbert, S.; Malacria, M. Efficient Preparation of Functionalized Hybrid Organic/Inorganic Wells-Dawson-Type Polyoxotungstates. *J. Am. Chem. Soc.* **2005**, *127*, 6788−6794.
(67) Nair, D. P.; Podgórski, M.; Chatani, S.; Gong, T.; Xi, W.; Fenoli, C. R.; Bowman, C. N. The Thiol-Michael Addition Click Reaction: A Powerful and Widely Used Tool in Materials Chemistry. *Chem. Mater.* **2014**, *26*, 724−744.
(68) Hoyle, C. E.; Bowman, C. N. Thiol-Ene Click Chemistry. *Angew. Chem., Int. Ed.* **2010**, *49*, 1540−1573.
(69) Chorghade, G. S.; Pope, M. T. Heteropolyanions as Nucleophiles. 1. Synthesis, Characterization, and Reactions of Keggin- and Dawson-Type Tungstostannates(II). *J. Am. Chem. Soc.* **1987**, *109*, 5134−5138.
(70) Bassindale, A. R.; Liu, Z.; MacKinnon, I. A.; Taylor, P. G.; Yang, Y.; Light, M. E.; Horton, P. N.; Hursthouse, M. B. A Higher Yielding Route for T8 Silsesquioxane Cages and X-Ray Crystal Structures of Some Novel Spherosilicates. *Dalton Trans.* **2003**, 2945−2949.
(71) Cheng, S. Z. D. *Phase Transitions in Polymers: The Role of Metastable States*, 1st ed.; Elsevier: Amsterdam, 2008.
(72) Chen, Q.; Bae, S. C.; Granick, S. Directed Self-Assembly of a Colloidal Kagome Lattice. *Nature* **2011**, *469*, 381−384.
(73) Mizuno, N.; Yamaguchi, K.; Kamata, K. Epoxidation of Olefins with Hydrogen Peroxide Catalyzed by Polyoxometalates. *Coord. Chem. Rev.* **2005**, *249*, 1944−1956.
(74) Katsoulis, D. E. A Survey of Applications of Polyoxometalates. *Chem. Rev.* **1998**, *98*, 359−388.
(75) He, T.; Yao, J. Photochromism in Composite and Hybrid Materials Based on Transition-Metal Oxides and Polyoxometalates. *Prog. Mater. Sci.* **2006**, *51*, 810−879.
(76) Clemente-Juan, J. M.; Coronado, E. Magnetic Clusters from Polyoxometalate Complexes. *Coord. Chem. Rev.* **1999**, *193*, 361−394.
(77) Rhule, J. T.; Hill, C. L.; Judd, D. A.; Schinazi, R. F. Polyoxometalates in Medicine. *Chem. Rev.* **1998**, *98*, 327−358.

DOI: 10.1021/acsnano.6b01336
ACS Nano 2016, 10, 6585−6596